Supplementary Information (SI) for EES Solar.

Supporting Information

Solution Processed Metal-Oxide:Polymer Interlayer Improves Perovskite Photodetector Response Speed, Dark Current, and Stability

Carlo A.R. Perini[1]*, Giorgio Ferrari[2], Juan-Pablo Correa-Baena[1,3], Annamaria Petrozza[4], Mario Caironi[4]*

[1] School of Materials Science and Engineering, Georgia Institute of Technology, Atlanta, GA, 30332 USA

[2] Department of Physics, Politecnico di Milano, Milan, 20133 Italy

[3] School of Chemistry and Biochemistry, Georgia Institute of Technology, Atlanta, GA, 30332 USA

[4] Center for Nano Science and Technology, Istituto Italiano di Tecnologia, Milan, 20134 Italy

*carperini@gatech.edu, mario.caironi@iit.it

Materials and Methods

Device Fabrication

To prepare $MAPbI_3$, methylammonium iodide (CH_3NH_3I, Dyesol), lead iodide (PbI_2, 99.9985 %, Alfa Aesar), and dimethyl sulfoxide (DMSO, anhydrous, 99.8 %, Sigma-Aldrich) were combined in 1 mL of dimethylformamide (DMF, anhydrous, 99.8 %, Sigma-Aldrich) to achieve a 1 M concentration. The mixture was stirred at 60 °C until fully dissolved. For the ZnO:PFN solution, 1 mg mL^{-1} of PFN (Solarmer Materials) was dissolved in methanol (Sigma-Aldrich) with 0.4 wt % acetic acid (Sigma-Aldrich), and the solution was stirred overnight. The resulting solution was filtered using a 0.2 µm PTFE filter, and then mixed with a commercial ZnO solution (N-10x, Nanograde ink) at a 1:3 v/v ratio.

Glass substrates coated with Indium-doped Tin Oxide (ITO, XoFisica, 15 Ω sq^{-1}, 2.8 x 2.8 cm^2) were patterned using zinc powder and a 2M hydrochloric acid (HCl) solution. Afterward, the substrates were cleaned by sonication in a 2 % v/v aqueous solution of Hellmanex III (Sigma-Aldrich) for 10 minutes. This was followed by sequential cleaning steps in deionized water (twice), isopropanol (IPA), acetone, and IPA, with each step lasting 10 minutes. Poly(3,4-ethylenedioxythiophene):polystirene sulfonate (PEDOT:PSS, Clevios P VP Al4083, Heraeus), filtered through a 0.22 µm PVDF filter, was then spin-coated onto the oxygen plasma-treated substrates (6 min) at 4000 rpm for 40 s. The coated substrates were subsequently annealed at 150 °C for 10 min, and immediately transferred to a N_2 glovebox. Then, the $MAPbI_3$ solution was filtered through a 0.22 µm PTFE filter and spin-coated on the substrates at 4000 rpm for 15 s. After 9 s into the spin-coating process, 300 µl of anhydrous toluene (99.8 %, Sigma-

Aldrich) was dripped onto the rotating substrate. The film was then annealed at 100 °C for 10 min, to remove residual solvents and promote crystallization. For the deposition of the electron transport layer (ETL), a $PC_{61}BM$ solution (NanoC, 30 mg mL^{-1} in chlorobenzene) was filtered through a 0.22 µm PTFE filter and spin-coated at 1000 rpm for 40 s. An annealing step at 60 °C for 40 s was performed to remove any remaining solvent. Either ZnO:PFN or AZO (N-21x, Nanograde ink) was then deposited by spin-coating at 1000 rpm for 40 s. The photodetectors were finalized by thermally evaporating a 75 nm aluminum cathode.

Characterization

Current density-voltage (J-V) curves under light were recorded under simulated AM 1.5 AAA illumination using a solar simulator from Newport and a scan rate of 100 mV s^{-1}. Devices were masked to define an illumination area of 0.0935 cm^2.

Dark J-V characteristics were obtained using an Agilent B1500 Semiconductor Parameter Analyzer, with voltage sweeps conducted at low scan rates (< 10 mV s^{-1}) in both forward and reverse directions. The measured current was normalized to the active area of the detector (0.16 cm^2).

Linear Dynamic Range (LDR) measurements were conducted by irradiating the device with a 450 nm laser, mechanically chopped at 133 Hz. Neutral density filters were used to attenuate the light, and the optical power on the device was calibrated with a silicon photodiode and power meter. The photogenerated signal was amplified by a transimpedance amplifier that also biased the device at -0.1 V, and the signal was read via a lock-in amplifier. The intensity range explored was limited by the setup, allowing only a lower estimate of the LDR, as the devices maintained a linear response throughout the measurement. The LDR was calculated as LDR = 20 $\log_{10}$ ($I_{max,\ meas}$ / $I_{min,\ meas}$), where $I_{max,\ lin}$ represent the maximum photogenerated current for which the device preserves an unchanged R, and $I_{min\ meas,\ lin}$ is the lowest measured current for which the responsivity (R) is preserved, which is higher than the actual lowest photocurrent at which linearity is preserved, due to the limited measurement capabilities of our experimental setup.

External Quantum Efficiency (EQE) measurements were conducted using a custom-built system that included a tungsten-halogen lamp, an Oriel Apex monochromator illuminator, and a Keithley 2300 source meter. A Newport Silicon Photodiode (UV-818) was employed for calibration. No bias was applied on the detectors during the EQE measurement.

Temporal response measurements were performed in a glovebox, using a train of 500 µs long light pulses (1 ms period, 2.94 mW cm^{-2} power) generated by a 630 nm LED driven by a Keysight 81150A function generator. The transient photocurrent from the device, biased at -0.1 V, was amplified by a transimpedance amplifier (Femto, DHPCA-100) and recorded on a Tektronix MSO4054 oscilloscope.

Noise current power spectra were recorded in the dark and in air, with the device biased at -0.1 V. A custom correlation spectrum analyzer was used for data acquisition.[1] The setup included two measuring channels connected to the electrodes of the device under test (DUT) to eliminate uncorrelated noise added by the instrument. The Fourier transform of the signal acquired with the first channel is multiplied by the complex conjugate of the Fourier transform of the second channel. The operation is repeated many times, and the results are averaged to obtain a more precise power spectral density. Figure S10 presents a schematic of the setup used for the measurement. A photodiode of 5.25 mm^2 area was used for this measurement. The measurement setup had a C_{stray} of 25 pF, a C_i of 5 pF, and a R_f of 4 MΩ.

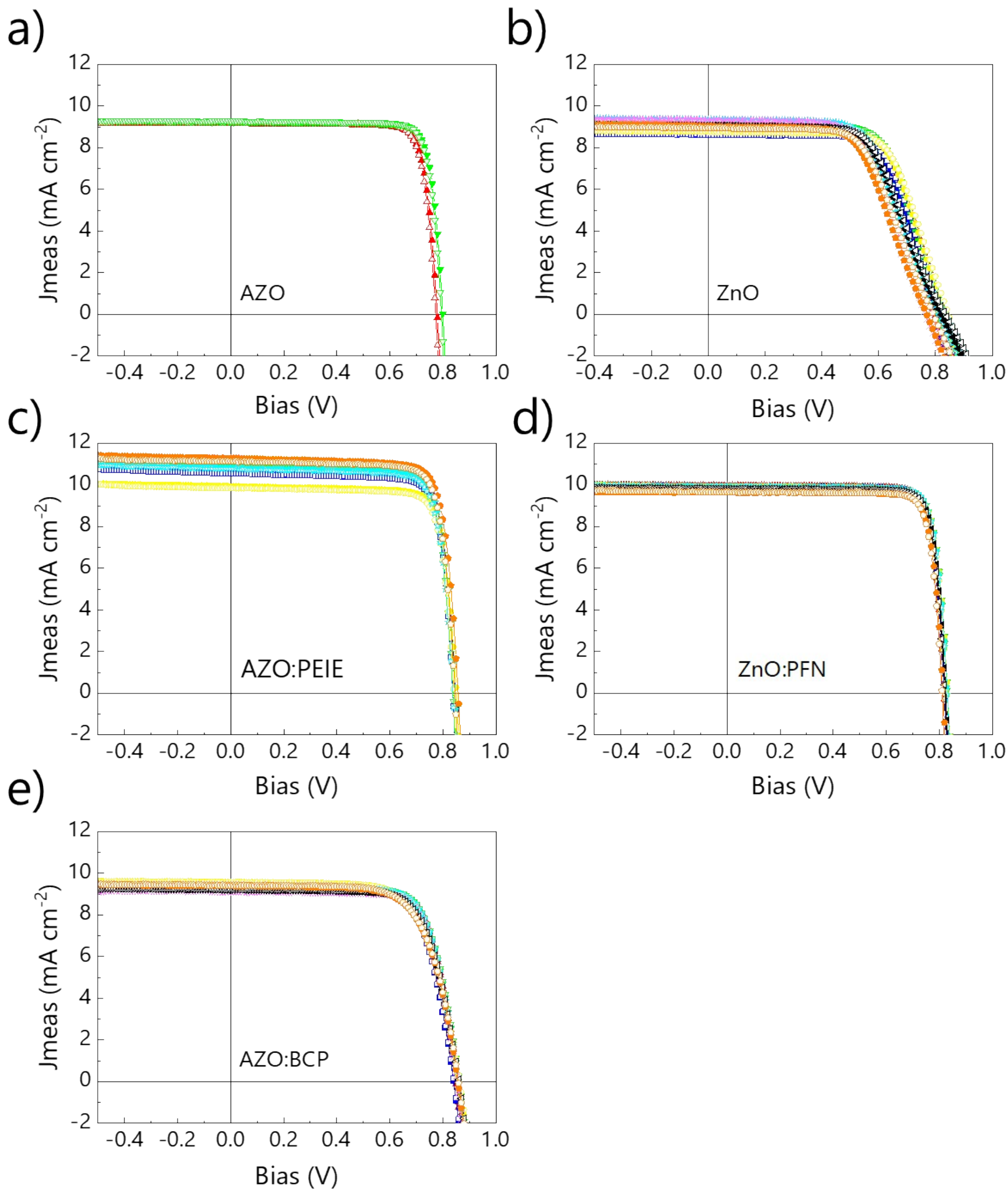

Figure S1. *J-V* curves under AM1.5 illumination in forward (hollow symbols) and reverse bias (solid symbols) scan direction. Multiple devices are presented in each plot as *J-V* curves with different color.

Table S1. Series (R_s) and shunt resistance (R_{sh}) extracted from the forward *J-V* scan under illumination of the most efficient pixel for each variation. R_{sh} was retrieved from the slope of the *J-V* around J_{SC}. R_s was retrieved from the slope of the curve around V_{OC}. R_s was not retrieved for the ZnO device due to the presence of S-shape in the curve affecting the slope near V_{OC}.

	AZO	ZnO	AZO:PEIE	ZnO:PFN	AZO:BCP
R_s (Ω cm^2)	4.3	n.a.	4.3	4.1	11
R_{sh} (kΩ cm^2)	17	5	7	50	50

Supplementary Note 1. In photodiodes, the series and shunt resistance represent indirect indicators of the range of incident optical powers that can be measured by the detector, i.e. its dynamic range. A high shunt resistance in a photodiode reduces white noise contributions from both shot noise and Johnson noise, enabling lower power optical signals to be detected. A low series resistance increases the threshold value at which space charge effects arise and limit charge extraction, allowing the detection of higher power optical signals before responsivity losses are observed. A lower series resistance also aids the frequency response of the detector, as the circuital limitation of the f^{ckt}_{-3dB} – the frequency of an incident optical signal at which the output of the detector decreases of -3 dB (~70.7%) with respect to its static response – can be expressed as:[2]

$$\left(f^{ckt}_{-3dB}\right)^{-2} \cong \left(\frac{1}{2\pi C_g R_s}\right)^{-2},$$

where C_g is the detector capacitance.

Supplementary Note 2. As shown in Figure S2, a photodiode in quasi-static condition can be represented by neglecting capacitive components in the circuit as a parallel of a diode and a shunt resistance, in series with a series resistance R_s.[3] The R_{sh} dominates the response of the system before the diode reaches its threshold voltage (V_{th}) allowing leakage current to pass. Once V_{th} is reached, the current flowing through the diode is much larger than the current flowing through the shunt resistance, and the dark *J-V* is dominated by the diode. As currents flowing through the photodiode increase, the voltage drop on resistive components starts to dominate the system, which is normally observed as a deviation from linearity at higher biases when the diode *J-V* scan is plot in semilogarithmic scale. For the diode dominated region, it holds the equation:

$$J_{dark}(V) = J_0\left(e^{\frac{qV}{nk_BT}} - 1\right),$$

where J_0 is a constant, V is the applied bias, n is called *ideality factor* and accounts for non-ideal behaviors of the diode (eg. non-radiative recombination), k_B is Boltzmann constant, and T is the temperature. For an ideal diode, $n = 1$ holds, while a system dominated by non-radiative recombination is usually characterized by $n = 2$.[4] Using the above simplifications, we can use a linear fit to *the J-V* curve at negative and small positive voltages to extract R_{sh}, a linear fit at high bias values can be used to retrieve R_s, and a linear fit on a Log (J)-V plot can be used to retrieve n from the slope of the fit using the equation:

$$n = \frac{q}{mk_BT}\log e,$$

where q is the electron charge, m is the slope retrieved from the fit, k_B is Boltzmann constant, T is 293 K, and the logarithm of e is used to convert the logarithm from base 10 to base e.

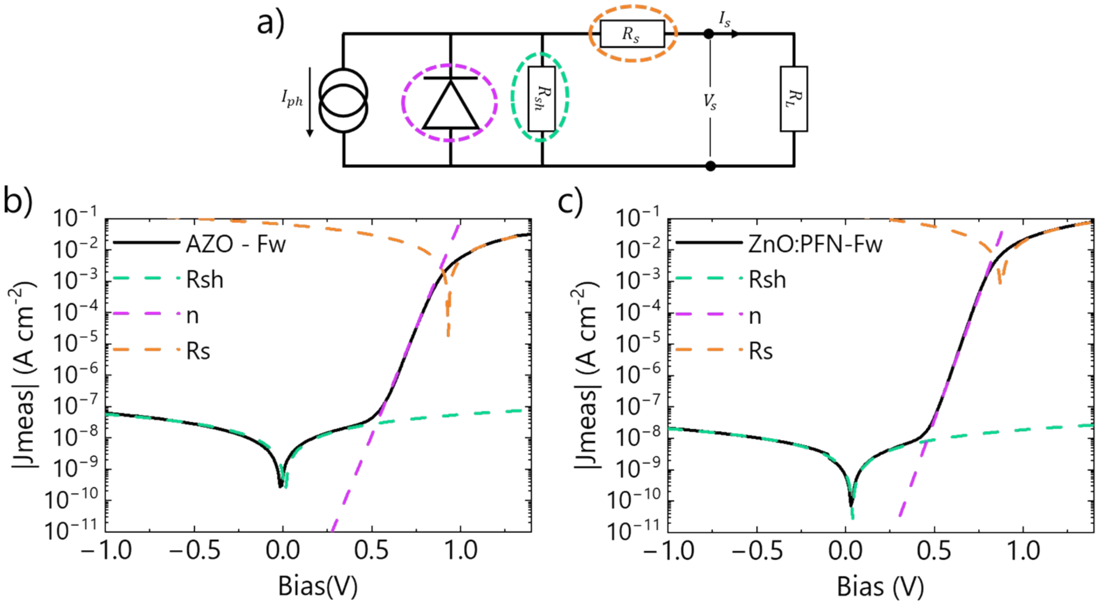

Figure S2. a) Quasi-static electrical equivalent model used to extract the values of R_{sh}, R_S, n. b) Fits of R_{sh}, R_S, n for the AZO detector. c) fits of R_{sh}, R_S, n for the ZnO:PFN detector.

Table S2. Values of shunt and series resistance extracted from the Dark J-Vs forward scan.

	AZO	ZnO:PFN
R_s (Ω cm^2)	14.3	6.7
R_{sh} (MΩ cm^2)	17.2	51.3
n	1.25	1.09

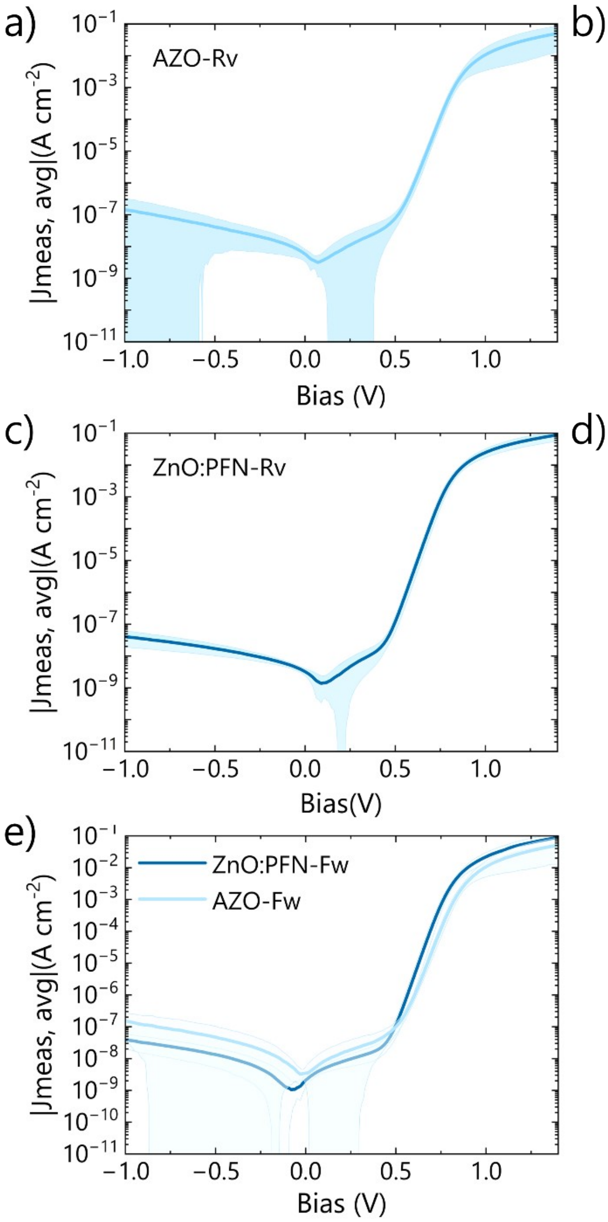

Figure S3. Statistics for the dark *J-V* scans of 7 AZO and 6 ZnO:PFN detectors acquired using a scan speed below 10 mV s^{-1}. AZO reverse scan (a), forward scan (b) and ZnO:PFN reverse scan (c) and forward scan (d). Comparison of the forward scan of AZO and ZnO:PFN detectors (e). Solid line is the average, while shaded area represents the standard deviation.

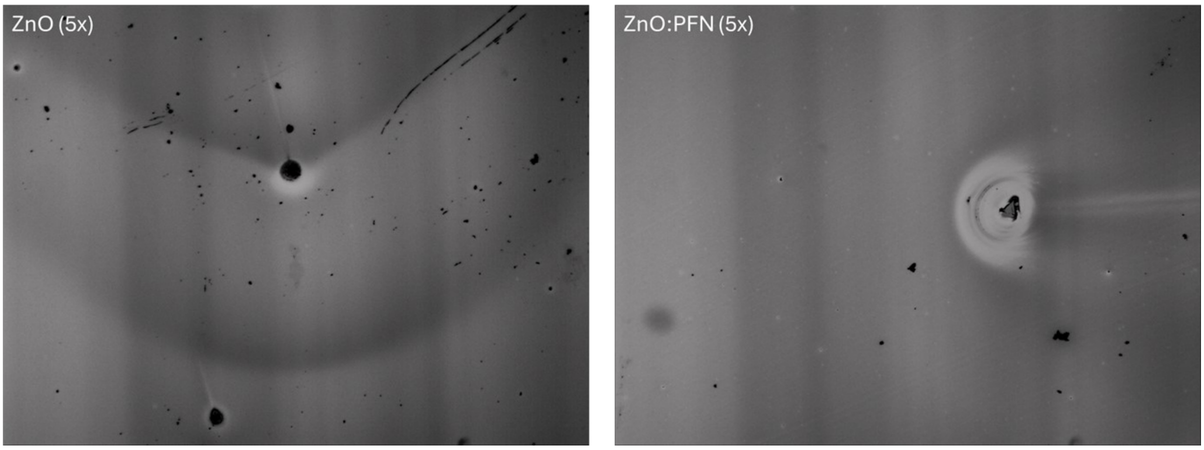

Figure S4. Microscope images of ZnO and ZnO:PFN films deposited on top of $MAPbI_3$ taken at a 5x magnification. Large comets due to defects in the underlying films are observed when ZnO-only is deposited, reducing the layer uniformity, while these effects are significantly reduced in ZnO:PFN films.

Table S3. Cutoff frequency as a function of area for the perovskite photodiodes incorporating an AZO or a ZnO:PFN interlayer.

Area (mm²)	**15.67**	**10.53**	**5.53**	**1.51**
f_{-3dB}^{AZO} (MHz)	0.2	0.3	0.8	1.4
$f_{-3dB}^{ZnO:PFN}$ (MHz)	0.3	0.5	0.9	2.1

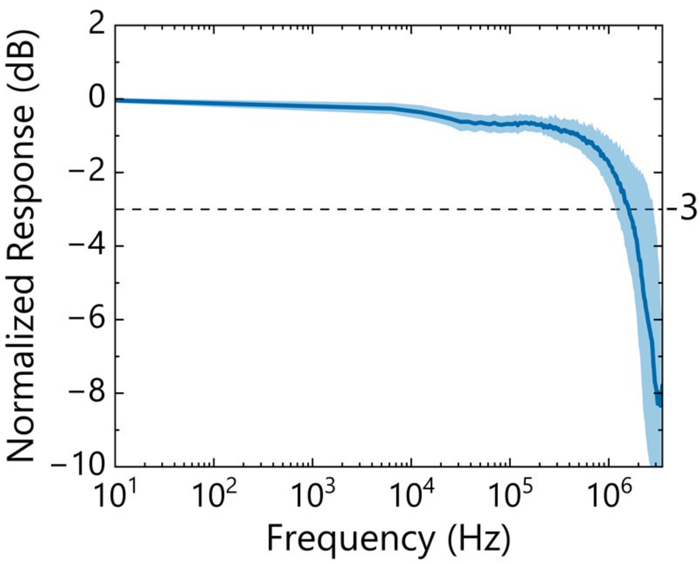

Figure S5. Frequency response of 5 x 1.51 mm^2 ZnO:PFN detectors. Solid line is the average, standard deviation is the shaded area.

Supplementary Note 3. The f_{-3dB} of a photodiode can be expressed as composed of a circuit-limited component and a transit time limited term:[2]

$$(f_{-3dB})^{-2} = (f_{-3dB}^{ckt})^{-2} + (f_{-3dB}^{tr})^{-2},$$

where f_{-3dB}^{ckt} is the cutoff frequency determined by the capacitive and resistive components of the diode, and f_{-3dB}^{tr} is the cutoff frequency determined by the transit time of carriers. As the capacitive contributions of the circuit are reduced, the system total cutoff frequency (f_{-3dB}) increases proportionally, until f_{-3dB}^{ckt} approaches f_{-3dB}^{tr}. As f_{-3dB}^{ckt} approaches f_{-3dB}^{tr}, the gains in f_{-3dB} reduce, and f_{-3dB} asymptotically approaches f_{-3dB}^{tr}. We show an example of this trend in Figure S6a, where we set a f_{-3dB}^{tr} of 10^7 Hz. Assuming f_{-3dB}^{ckt} to be inversely proportional to the device area, the evolution of f_{-3dB} versus the reciprocal of the device area should follow an analogous trend to the one show in Figure S6a. As shown in Figure S6b, the f_{-3dB} of photodiodes incorporating the AZO interlayer appear to begin to saturate, while it remains unclear whether the detectors including the ZnO:PFN layer are approaching saturation (Figure S6c).

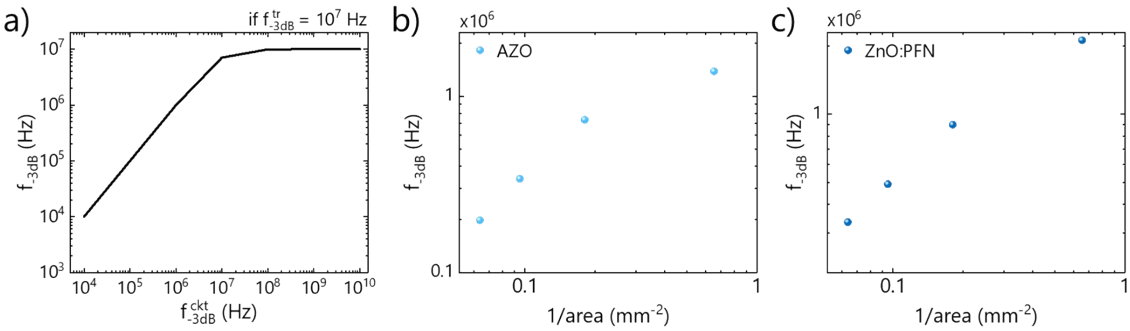

Figure S6. a) Cutoff frequency of a photodetector with intrinsic cutoff at 10^7 Hz as a function of circuital cutoff frequency. b) Cutoff frequency as a function of area for the AZO detector. c) f_{-3dB} as a function of area for the ZnO:PFN detector.

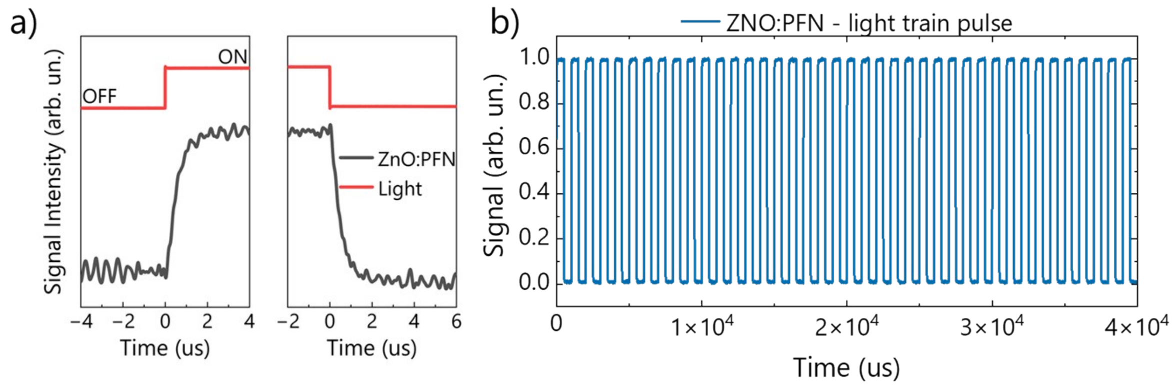

Figure S7. a) Rise and Fall of the ZnO:PFN photodetector signal in response to a rectangular light pulse 500 μs long. b) Photoresponse of the ZnO:PFN detector to a train of rectangular light pulses.

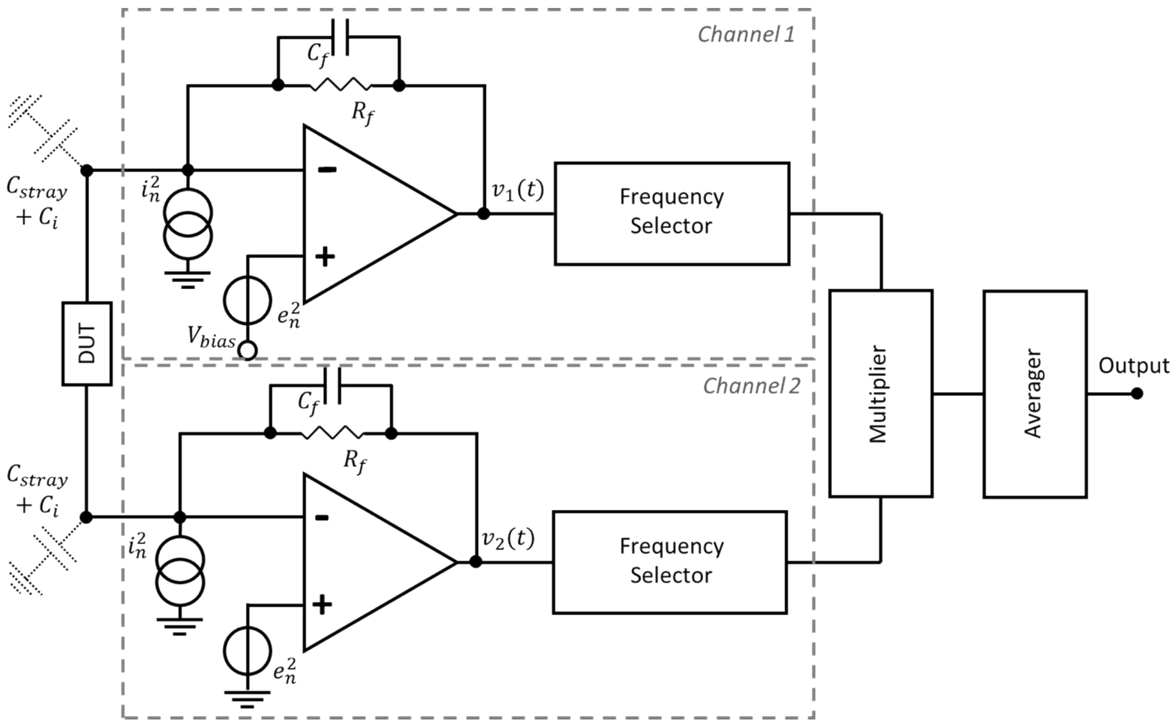

Figure S8. Schematic of the noise measurement setup showing the connection of the photodetector (Device Under Test – DUT), and the two readout channels.[1]

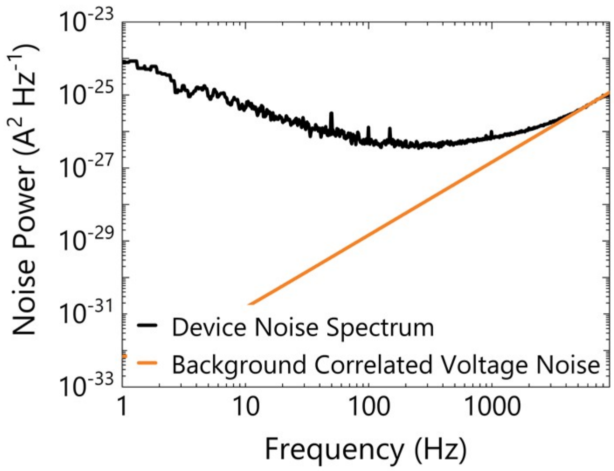

Figure S9. Expected background correlated voltage noise from the measurement setup (orange) and measured photodiode noise (black).

Area [mm^2]	Dark Current [A cm^{-2}] @-0.5V	Dark Current [A cm^{-2}] @-1V	Cutoff freq. [Hz]	Year	Perovskite	Evap. interlayer	HTL	ETL	Ref.
1.5	1.1E-08	2.1E-08	2.1E-06	--	$MAPbI_3$	No	PEDOT:PSS	PCBM | ZnO:PFN	**This work**
20	4.8E-10	1.0E-09	5.0E+05	2015	$MAPbI_3$	Yes	PEDOT:PSS	PCBM | C_{60} | LiF	5
6	5.0E-10	1.0E-09	1.0E+04	2023	$MAPbI_3$	Yes	NiOx	PCBM | ZnO | BCP	6
6	4.8E-10	7.0E-10	1.2E+04	2024	$MAPbI_3$	Yes	NiOx | PMMA	PMMA | PCBM | ZnO | BCP	7
0.5	6.0E-08	1.4E-07	3.5E+06	2018	$MAPbI_3$	No	PEDOT:PSS	PCBM | AZO	8
20	5.0E-08	--	3.5E+05	2015	$MAPbBrI_2$	Yes	PEDOT:PSS	C_{60} | LiF	9
7.25	2.7E-09	4.2E-09	2.9E+06	2015	$MAPbI_3$	Yes	OTPD	PCBM | C_{60} | BCP	10
10	2.0E-06	--	6.5E+04	2017	$FA_{0.83}Cs_{0.17}Pb(I_{0.9}Br_{0.1})_3$+CyPF6	No	PEDOT:PSS	PCBM	11
0.6	1.0E-07	--	1.2E+06	2017	$MAPbI_3$	Yes	PTAA	C_{60} |BCP	12
0.6	1.0E-09	--	3.2E+06	2017	$MAPbBr_3$	Yes	PTAA	C_{60} |BCP	12
10	3.0E-07	2.0E-06	1.1E+05	2016	$MAPbI_3$	No	Spiro-OMeTAD	TiO_2	13
4.5	2.2E-07	3.7E-07	2.2E+05	2018	$FAPbI_3$	No	Spiro-OMeTAD	TiO_2	14
9	1.0E+08	1.0E-07	1.0E+04	2018	$CsPbI_3$	Yes	P3HT | MoO_3	ZnO	15
1	1.7E-08	8.6E-08	2.9E+06	2014	$MAPbI_{3-x}Cl_x$	No	PEDOT:PSS	PCBM | PFN	16
--	2.0E-08	--	6.0E+04	2022	$MAPbI_3$	No	MeO-2PACz	PCBM | BCP	17
--	2.0E-09	--	7.0E+04	2022	$MAPbI_{2.55}Br_{0.45}$	No	MeO-2PACz	PCBM | BCP	17

Table S4. Literature review of perovskite photodiodes dark currents and cutoff frequencies.

--	2.0E-07	--	7.8E+2	2022	$MAPbI_{2.25}Br_{0.75}$	No	MeO-2PACz	PCBM | BCP	17

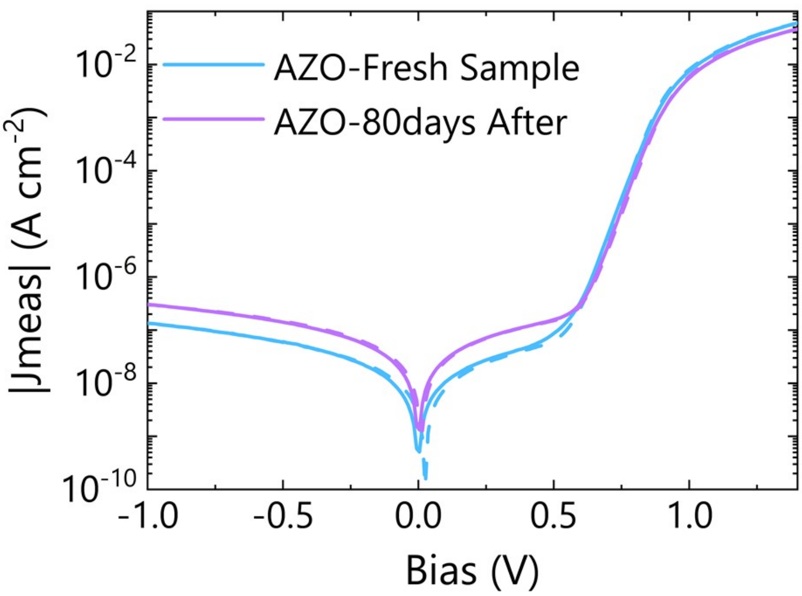

Figure S10. Dark *J-V* of the MHP photodetector with the AZO interlayer as prepared (blue) and after 80 days aging in N2 atmosphere (purple). Forward scans are presented as solid lines, while the reverse scans are dashed.

References

1 G. Ferrari and M. Sampietro, Correlation spectrum analyzer for direct measurement of device current noise, *Review of Scientific Instruments*, 2002, **73**, 2717.

2 S. Donati, Photodetectors: Devices, Circuits, and Applications, *Meas Sci Technol*, 2001, **12**, 653–653.

3 Jenny Nelson, *The Physics of Solar Cells*, Imperial College Press, London, First., 2004.

4 W. Tress, M. Yavari, K. Domanski, P. Yadav, B. Niesen, J. P. C. Baena, A. Hagfeldt, M. Graetzel, J. P. Correa Baena, A. Hagfeldt and M. Graetzel, Interpretation and evolution of open-circuit voltage, recombination, ideality factor and subgap defect states during reversible light-soaking and irreversible degradation of perovskite solar cells, 2018, **11**, 151–165.

5 Q. Lin, A. Armin, D. M. Lyons, P. L. Burn and P. Meredith, Low noise, IR-blind organohalide perovskite photodiodes for visible light detection and imaging, *Advanced Materials*, 2015, **27**, 2060–2064.

6 J. Park, Y. Aggarwal, W. Kim, S. Sharma, E. H. Choi and B. Park, Self-powered CH 3 NH 3 PbI 3 perovskite photodiode with a noise-suppressible passivation layer of poly(methyl methacrylate) , *Opt Express*, 2023, **31**, 1202.

7 Y. Aggarwal, J. W. Park, W. Kim, S. Sharma, H. R. Jeong, M. G. Kim, J. Kil, E. H. Choi and B. Park, Highly efficient self-powered CH3NH3Pbl3 perovskite photodiode with double-sided poly(methyl methacrylate) passivation layers, *Solar Energy Materials and Solar Cells*, DOI:10.1016/j.solmat.2024.112815.

8 C. A. R. Perini, A. J. Barker, M. Sala, A. Petrozza and M. Caironi, High speed solution-processed hybrid perovskite photodetectors with low dark current enabled by a low temperature metal oxide interlayer, *Semicond Sci Technol*, 2018, **33**, 094004.

9 Q. Lin, A. Armin, P. L. Burn and P. Meredith, Filterless narrowband visible photodetectors, *Nat Photonics*, 2015, **9**, 687–694.

10 Y. Fang and J. Huang, Resolving weak light of sub-picowatt per square centimeter by hybrid perovskite photodetectors enabled by noise reduction, *Advanced Materials*, 2015, **27**, 2804–2810.

11 Q. Lin, Z. Wang, M. Young, J. B. Patel, R. L. Milot, L. Martinez Maestro, R. R. Lunt, H. J. Snaith, M. B. Johnston and L. M. Herz, Near-Infrared and Short-Wavelength Infrared Photodiodes Based on Dye–Perovskite Composites, *Adv Funct Mater*, DOI:10.1002/adfm.201702485.

12 C. Bao, Z. Chen, Y. Fang, H. Wei, Y. Deng, X. Xiao, L. Li and J. Huang, Low-Noise and Large-Linear-Dynamic-Range Photodetectors Based on Hybrid-Perovskite Thin-Single-Crystals, *Advanced Materials*, 2017, **29**, 1–7.

13 S. Casaluci, L. Cina, F. Matteocci, P. Lugli and A. Di Carlo, Fabrication and Characterization of Mesoscopic Perovskite Photodiodes, *IEEE Trans Nanotechnol*, 2016, **15**, 255–260.

14 M. Zhang, F. Zhang, Y. Wang, L. Zhu, Y. Hu, Z. Lou, Y. Hou and F. Teng, High-Performance Photodiode-Type Photodetectors Based on Polycrystalline Formamidinium Lead Iodide Perovskite Thin Films, *Sci Rep*, DOI:10.1038/s41598-018-29147-6.

15 K. M. Sim, A. Swarnkar, A. Nag and D. S. Chung, Phase Stabilized α-CsPbI3 Perovskite Nanocrystals for Photodiode Applications, *Laser Photon Rev*, DOI:10.1002/lpor.201700209.

16 L. Dou, Y. M. Yang, J. You, W. Chang, G. Li, Z. Hong and Y. M. Yang, Solution-processed hybrid perovskite photodetectors with high detectivity, *Nat Commun*, 2014, **5**, 1–6.

17 F. Furlan, D. Nodari, E. Palladino, E. Angela, L. Mohan, J. Briscoe, M. J. Fuchter, T. J. Macdonald, G. Grancini, M. A. McLachlan and N. Gasparini, Tuning Halide Composition Allows Low Dark Current Perovskite Photodetectors With High Specific Detectivity, *Adv Opt Mater*, DOI:10.1002/adom.202201816.